

**SCALE INTERACTIONS IN AN URBAN-LIKE BOUNDARY LAYER:
A WIND TUNNEL STUDY**

CÉDRIC RIVET ^{*}, LAURENT PERRET AND JEAN-MICHEL ROSANT
LUNAM Université, École Centrale de Nantes, LHEEA - UMR CNRS 6598.

ABSTRACT

The aim of the present study is to elucidate the spatio-temporal interactions between the atmospheric boundary layer and the flow developing in an urban canopy layer. To do so, a full-depth simulation of a suburban BL above an idealized canopy model is performed in a wind tunnel. The dynamics of this flow is investigated in a stream-wise aligned vertical plane via Stereoscopic Particle Image Velocimetry (SPIV). Focusing on the high shear region just downstream of a roughness element, two flow configurations are identified depending on the angle of the shear layer against the horizontal axis. This parameter proves to be a good indicator of the flow dynamics and the mutual influence between the canopy layer and the boundary layer flows. The main findings of the present work are that the top-down interaction between the two flows is confirmed but also that, thanks to the detection of the vortex clusters shed from the roughness elements, the roughness sublayer is populated by strong vortical structures which originate from the canopy layer. These vortices are accompanied with ejection and sweep events and are found to contaminate the boundary layer.

1 INTRODUCTION

The study of turbulence in a boundary layer (BL) over a city is needed to understand the transport processes of mass, momentum and passive scalar. These processes are related to the properties of the mean flow but also to the spatio-temporal dynamics of the flow.

^{*} *Corresponding author address:* Cédric Rivet, LUNAM Université, École Centrale de Nantes, LHEEA - UMR CNRS 6598, 1 rue de la Noe, BP 92101, 44321 Nantes Cedex 3, France.

Existence of universal features, in the inertial sublayer and the outer region of turbulent BL, has been suggested by Raupach (1981). Over thirty years of studies on smooth-wall BL have resulted in a consensus based on a vortex organization model in the outer region summarized by Adrian et al. (2000b). Coherent structures identified in this model, such as low-speed streaks (or low momentum region, Tomkins and Adrian 2003), seem to exist over rough-wall independently of its nature. LES (Kanda et al. 2004, Kanda 2006) studies over cube arrangements showed that the low speed streaks are similar to those over a smooth wall. However, in the roughness sublayer (RSL), turbulence mechanisms depend on the nature of the roughness elements (Krogstad and Antonia 1999). Castro et al. (2006) confirmed the influence of the roughness elements. A two-scale behaviour has been evidenced: small-scale eddies, less than the mean height of the obstacles in size, generated by the separated shear layers and larger-scale structures from the BL flow indeed leave their imprints in the two-point correlation of the longitudinal velocity (see Castro et al. 2006). These two types of organized structures are dominated by sweep and ejection events (see models from Adrian et al. 2000b and Inagaki 2008) responsible for turbulent exchanges.

Focusing on the flow dynamics within and over a staggered cube array, Coceal et al. (2007a) found from their DNS results that eddies shed off the vertical edges of the obstacles are rotated by mean shear. Furthermore, strong canopy-top shear layers were found to intermittently penetrate into the canopy layer (CL), impacting upon downstream obstacles and driving a recirculation in front of the obstacles. Takimoto et al. (2011) described the existence of two characteristic modes from the analysis of the flow over a squared cube array: flushing and cavity-eddy modes.

In their study of a high Reynolds number BL over a smooth wall, Hutchins and Marusic (2007) showed the existence of very large-scale motions consisting of meandering elongated low- and high-speed regions. These structures were found to play a significant role in redistributing small-scale turbulent motions throughout the BL.

Following Townsend’s original idea (Townsend 1956), Inagaki and Kanda (2010) and Castillo et al. (2011) used a spatial decomposition method to separate inner and outer layer turbulence and confirmed the influence of large-scale structures from the BL. Using the same approach, Perret and Ruiz (2012) evidenced the presence of very large-scale motions, meandering in the horizontal plane, in their wind tunnel simulation of an atmospheric BL over a vegetation canopy. Recently, Inagaki et al. (2012) suggested that the turbulent organized structures represented by low and high speed streaks control CL flow events such as flushing and cavity eddies. This relationship confirms a top-down mechanism (Hunt and Morrison 2000, Marusic et al. 2010).

Building on these previous results, the present study attempts to separate the flow developing above the CL in a large-scale part originating from the BL and a small-scale part corresponding to the emerging CL flow. Identification of the canopy-atmosphere interface is performed by detecting the axis of the shear layers which develop downstream of the roughness elements, characterized by the location of the maximum of the vertical gradient of instantaneous longitudinal velocity. Focusing on the flapping of this shear layer, two distinct flow configurations are highlighted. Conditional averaged velocity fields obtained for each configuration are analysed. Furthermore, detection of vortical structures via the computation of signed swirling strength maps reveals the presence of vortex cluster emanating from the roughness elements. The presence of such vortical structures in the RSL and above, and their relationships with Q2 and Q4 events are discussed.

2 EXPERIMENTAL SETUP

2.1 *Wind-tunnel*

Simulation of an urban BL over an idealized canopy model was performed in the atmospheric wind tunnel of the Laboratoire de recherche en Hydrodynamique, Energétique et Environnement Atmosphérique of Ecole Centrale de Nantes (LHEEA, Nantes, France). This facility is an

open-circuit suck-down tunnel which has working section dimensions of 24m long \times 2m wide \times 2m high (Fig. 2.1). The ceiling and lateral walls are transparent allowing optical access of the flow.

2.2 *Urban canopy model*

Inspired by the Counihan (1969) and Standen et al. (1972) simulation techniques, a full-depth simulation is performed using vertical mixing devices (a triangular tapered spires array, designed following the formulation of Irwin 1981), a non-castellated barrier normal to the flow and an idealized urban canopy model. This model is composed of a 22m long and 2m wide horizontal fetch of staggered wooden 0.05m high (h) cubic roughness elements with an homogeneous plan area density of 25%.

2.3 *Stereoscopic PIV setup*

In the following, x , y and z denote the longitudinal, the spanwise and the vertical directions, respectively, and u , v and w , the longitudinal, transversal and vertical velocities. Measurements of instantaneous three-component velocity fields were performed via SPIV.

The flow was seeded just downstream of the contraction with glycol/water droplets (typical size $1\mu\text{m}$) using a fog generator. With a 18.5m-long fetch, the test section was fully seeded. A 200mJ Nd:YAG Dual Power model laser operating at 532nm with a frequency of 5Hz was used to illuminate the particles between cubes from below the test section. The time delay between two images for PIV processing was set to $500\mu\text{s}$. 2048×2048 pixels compact DANTEC Dynamics FlowSense 4M cameras each equipped with a 105mm Nikon AF DC-NIKKOR objective lens, were mounted outside the wind tunnel on each side of the light-sheet. Measurements of the instantaneous three-component velocity were performed in a streamwise aligned vertical (x, z) plane (see Fig. 2.2). Parameters of this measurement configuration are summarized in Table 2.1. The Scheimpflug condition was satisfied by rotating the image plane with respect to the lens plane. To ensure this condition, the cameras were installed on special remote controlled mounts designed to enable the rotation between the lens and the CCD chip (using the DANTEC Remote Camera Control software). Both the synchronisation between the laser and the two cameras and the calculation of the PIV velocity vector fields were performed using the DANTEC Dynamics DynamicStudio software. After acquisi-

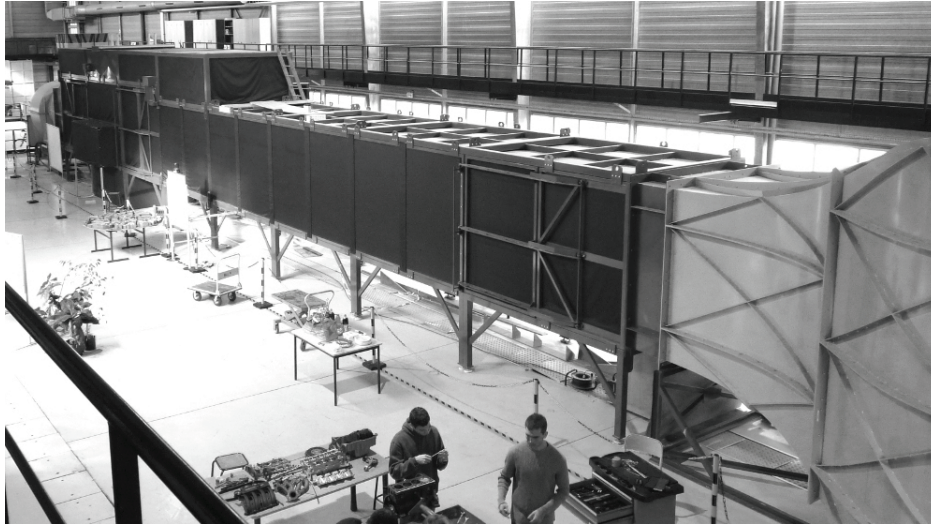


Figure 2.1: Photograph of the wind tunnel at LHEEA.

Table 2.1: PIV measurement parameters.

Field of view (h)	Spatial resolution (mm)	dt (μs)	Distance * (m)	Angle * ($^\circ$)
3.0 x 4.5	1.72 x 2.19	500	1.35	48

* : camera / lightsheet

tion, correction of lightsheet non-uniformities and deleting of static background artefacts were applied to the image pairs. An adaptive multi-pass cross-correlation algorithm was used with initial window size of 128×128 pixels and with 32×32 final interrogation windows and 50% overlap. Spurious vectors were detected by an automatic validation procedure whereby the SNR of the correlation peak had to exceed a minimum value of 1.2, and the vector amplitude had to be within a certain range of the local median to be considered as valid. Once spurious vectors had been detected, they were replaced by vectors resulting from a linear interpolation in each direction from the surrounding 3×3 set of vectors. The reconstruction of the third velocity component is based on the backprojected apparent in-plane displacements in the object plane for each camera using a pinhole camera model applied on five calibration images (for more details, see Adrian and Westerweel 2010). At last, 4,000 image pairs were recorded for this configuration.

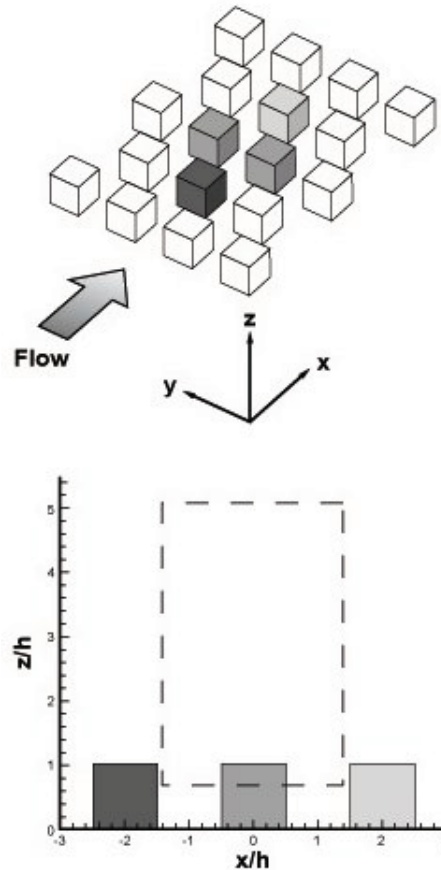
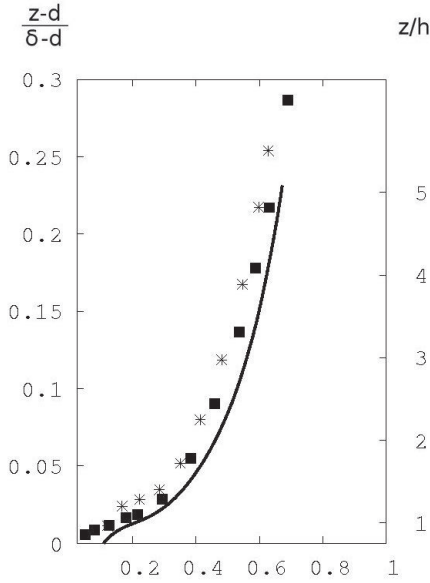


Figure 2.2: Configuration of measurement.

a)



b)

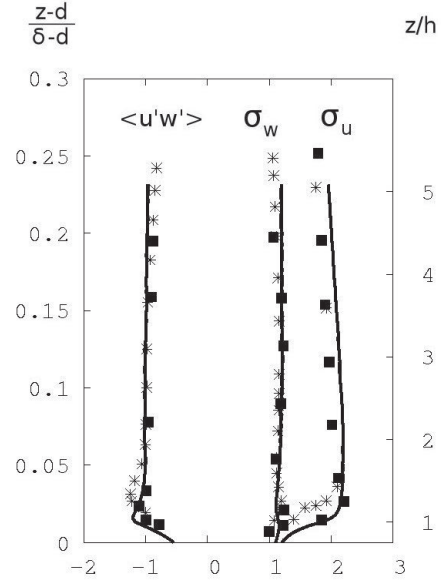


Figure 3.1: Vertical profiles of spatial averaged one-point statistics : a) longitudinal mean velocity normalized by U_e , b) standard deviations of the two in-plane components u and w normalized by u^* and Reynolds shear stress normalized by u^{*2} . Comparison between present SPIV measurements (line), DNS from Coceal et al. (2007b) (stars) and two-component PIV measurements from Reynolds and Castro (2008) (squares) with the same staggered arrangement and plan area density of roughness elements.

Table 3.1: Suburban boundary layer parameters.

δ/h	u^*/U_e	z_0/h	d/h	$Re_* = u^* h/\nu$
19.5	0.067	0.05	0.75	1260

3 RESULTS

In the following, using the Reynolds decomposition, the three components of the instantaneous velocity include a mean part symbolized by $\langle (\cdot) \rangle$ and a fluctuation part symbolized by $(\cdot)'$.

3.1 One-point statistics of the flow

Features of the simulated BL are determined for a longitudinal location $x = 18.5\text{m}$ from the start of the roughness fetch and a free stream velocity $U_e = 5.5\text{m}\cdot\text{s}^{-1}$.

In order to characterize the simulated turbulent boundary layer, a vertical profile of longitudinal mean velocity over the entire test section height was performed via hot wire anemometer, enabling the estimation of the boundary layer thickness δ over smooth wall ($\delta = 6h$) and over the urban

canopy model ($\delta = 19.5h$) (see Table 3.1). By fitting the longitudinal mean velocity measurements (belonging to the outer region) with a power law (eqn. 3.1) where d is the zero-plane displacement height, the nature of the simulated BL is confirmed. The value of the exponent α is indeed found to be $\alpha = 0.24$, which is characteristic of a BL flow developing over a suburban terrain ESDU (1972).

$$\frac{u(z)}{U_e} = \left(\frac{z-d}{\delta-d} \right)^\alpha \quad (3.1)$$

Due to some experimental limitations, the friction velocity u^* is estimated from the Reynolds shear stress $\langle u'w' \rangle$ value in the constant-flux region of the inertial sublayer (see Fig. 3.1.c) as $u^* = \sqrt{-\langle u'w' \rangle}$. In the same area, the roughness length z_0 is determined by fitting the longitudinal mean velocity measurements (i.e for $2 < z/h < 3$) with a logarithmic law (eqn. 3.2) using the values of d and u^* previously determined, and the von Karman constant $\kappa = 0.40$.

$$u(z) = \frac{u^*}{\kappa} \ln \left(\frac{z-d}{z_0} \right) \quad (3.2)$$

Figure 3.1 shows vertical profiles of the spatially averaged one-point statistics of the flow from

the SPIV measurements above the urban canopy model compared with results from the DNS of Coceal et al. (2007b) and the two-component PIV measurements of a wind tunnel simulation of Reynolds and Castro (2008) with the same staggered arrangement and plan area density of cubical obstacles. The present results are found to be in qualitative agreement with the two reference cases. As expected, standard deviations of fluctuation velocities show that the flow is clearly anisotropic near the CL where the longitudinal component mainly contributes to the turbulent kinetic energy, see Fig. 3.1.b. In the constant-flux region, the variation with height of the spatially averaged Reynolds shear stress does not exceed 4.5% (not shown). The upper limit of the RSL is estimated at $z/h = 2$ where the spatially averaged Reynolds shear stress quickly increases towards the roughness elements. A quadrant analysis (see Coceal et al. 2007b) shows dominance of Q2 and Q4 events throughout the inner region of the BL including the upper part of the CL. Our results (not shown here) are consistent with Coceal et al. (2007b): dominance (in number) of Q2 events in the RSL, balance of Q2 and Q4 events in the lower part of the constant-flux region, and dominance of Q4 events above $z/h = 3$. Although Q4 events are less numerous than Q2 ones at the canopy top, they contribute more to the Reynolds shear stress which shows a peak at the level of the top of the roughness elements (see Fig. 3.1.b).

3.2 Interface flow configurations

Observation of fluctuating velocity fields (see Fig. 3.2 for an example) allows to identify a two-scale behaviour of the flow as suggested by Castro et al. (2006). Above the RSL, large-scale movements and quasi-streamwise elongated coherent structures are dominant (large white arrow in Fig. 3.2). As described by Castro et al. (2006) and Coceal et al. (2007a), low-speed flow in the CL is populated by small-scale vortices generated by the shear layers emanating from top and lateral faces of roughness elements. At the interface, the local in-plane canopy-top shear layer is found to be intermittently downward, penetrating into the CL, and upward, extending in the RSL as shown in Fig. 3.2. Furthermore, this flapping shear layer seems to be correlated with vortices, independently of its tilt. In Fig. 3.2, the upward shear layer is correlated with a clockwise rotating vortex cluster (black arrows) and Q2 events (small white arrows). From the observation of numerous fluctuating ve-

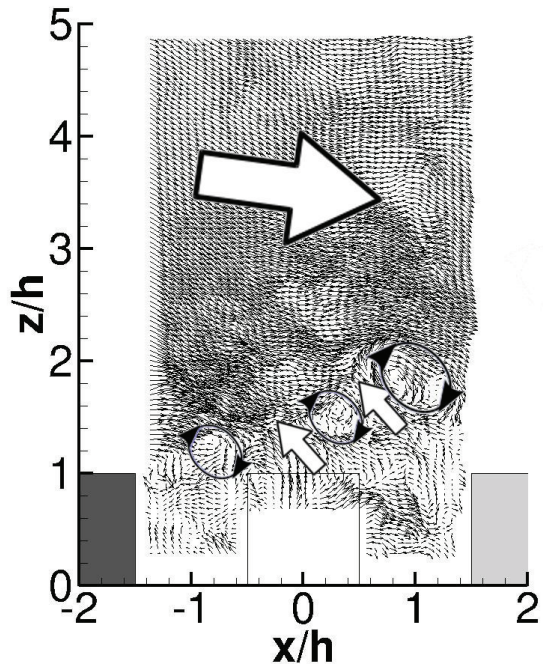


Figure 3.2: Example of a two-component vector field of the fluctuating velocity.

locity fields, the shear layer originating from an obstacle (upstream dark gray cube in figure 3.2) appears to be a good indicator of the dynamics of the flow in the RSL and of the interaction between the CL flow and the BL developing above. A basic feature of these shear layers is a high value of the instantaneous velocity gradient $\partial u/\partial z$. The location of the maximum of this velocity gradient $[\partial u/\partial z]_{max}$ is thus retained as an indicator of the shear layer axis, which will serve to identify the instantaneous interface between the CL flow and the overlying BL.

The mean tilt angle θ of $[\partial u/\partial z]_{max}$ with the horizontal plane, for $-1.5 < x/h < 0$, is estimated for each of the 4,000 instantaneous fields by fitting a straight line to the detected axis of the shear layer. Downstream of $x/h = 0$, due to the complex dynamics of the shear layer, the vertical dispersion of $[\partial u/\partial z]_{max}$ becomes too important to permit a good fit. This is less frequent for $-1.5 < x/h < 0$ but when it is the case, the fields are discarded. Figure 3.3 shows the probability density function (PDF) of θ . The PDF of θ is asymmetrical, the majority of tilt angles being found between -15° and 21° . In the CL, the multiple interactions between different shear layers

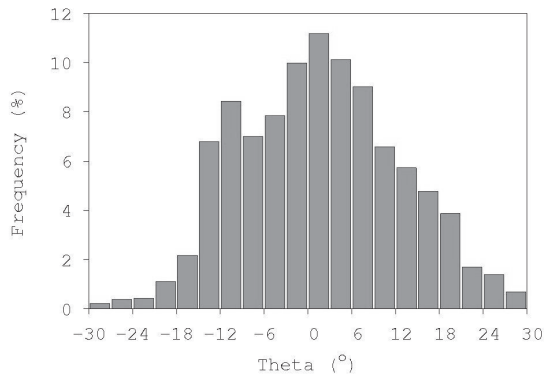


Figure 3.3: PDF of the mean tilt angle of $[\partial u/\partial z]_{max}$.

seem to prevent the canopy-top shear layer from having a stronger negative tilt. Furthermore, the height and arrangement of the roughness elements seem to limit the flapping of the cube-top shear layer. So, with a $3h$ -long (distance between the two in-plane cubes) shear layer and a characteristic maximum tilt angle about 20° , the downstream extremity of the shear layer reaches the ground (with a negative angle) or the top of the RSL (with a positive angle).

Building on these results, two different configurations are selected by isolating instantaneous fields respecting the following conditions :

$$\begin{aligned} \text{Positive tilt :} & \quad 11^\circ < \theta < 21^\circ \\ \text{Negative tilt :} & \quad -15^\circ < \theta < -5^\circ \end{aligned}$$

In both configurations, approximately 300 instantaneous velocity fields satisfy the conditions imposed on the shear layer tilt angle. Observation of instantaneous fields corresponding to the occurrence of one of these events shows a behaviour of the velocity components clearly different from the full ensemble averaged ones. In order to confirm these observations, a conditional averaged velocity field analysis of each configuration is performed.

3.3 Conditional averaged velocity fields

One-point statistics are computed for the two configurations and compared with the full ensemble averaged statistics from all the vector fields. Figure 3.4 mainly shows the two in-plane components of the mean velocity (two first rows) and the Reynolds shear stress (last row) as function of the normalized height z/h . The two first rows show that the conditioned mean flow is clearly marked by both selected configurations.

As expected, in the case of a positive tilt of the shear layer axis, the emergence of the low-speed flow from the CL is favored (Fig. 3.4.b and e). When $\theta > 0$, the $[\partial u/\partial z]_{max}$ region is correlated with a negative $\langle u'w' \rangle$ inclined area (blue patches in Fig. 3.4.h) which mainly corresponds to Q2 events (not shown). Above $2.5h$, $\langle u'w' \rangle$ is weaker than the full ensemble average (Fig. 3.4.g). In the RSL, this result suggests that a major part of the Q2 events are generated from the upward flapping of the shear layer created downstream of the roughness elements.

In the case of a negative tilt of the shear layer axis, the two in-plane components of the main velocity show a fast and large downward movement (Fig. 3.4.c and f). This phenomenon is more pronounced than the upward movement in the first conditional case and appears to be directly related to the BL flow developing above. However, the longitudinal mean velocity shows a lower speed upstream the downstream cube (light gray cube in figure 3.4). Statistically, the BL flow does not penetrate the CL over entire space between the two in-plane cubes. The CL flow moves statistically upward the upstream face of the downstream obstacle. This detail is not consistent with Coceal et al. (2007a) observations who show an opposite phenomenon. At last, the negative $\langle u'w' \rangle$ area shown in Fig. 3.4.i (large blue area) mainly corresponds to Q4 events (not shown) except for the close upstream area of downstream (light gray) cube.

3.4 Vortex cluster shedding

Focusing on the vortices shed off the top of the upstream cube, in-plane swirling strength (λ_{ci}) is estimated. Using the two-dimensional form of the velocity gradient tensor, the λ_{ci} is defined as the imaginary part of the quadratic solution when the solution is complex (Adrian et al. 2000a). In order to be able to discriminate between counter-clockwise and clockwise rotating vortices, λ_{ci} is multiplied by the sign of the local in-plane vorticity ω_y (Hutchins et al. 2005) such as :

$$\lambda_s = \lambda_{ci} \left(\frac{\omega_y}{|\omega_y|} \right). \quad (3.3)$$

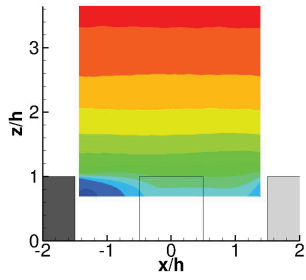
Maps of λ_s criterion show that vortices shed off the top of the upstream cube have high negative λ_s values. The PDF of λ_s is computed for all the 4,000 instantaneous fields as a function of height as shown in Fig. 3.5. Clockwise ($\lambda_s < 0$) and counter-clockwise ($\lambda_s > 0$) rotating vortices both

Full ensemble averages

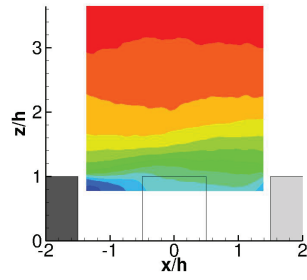
Positive tilt
of the shear layer axis

Negative tilt
of the shear layer axis

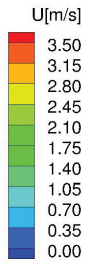
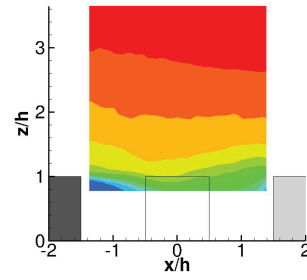
a)



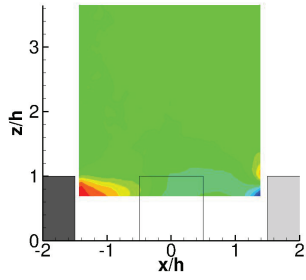
b)



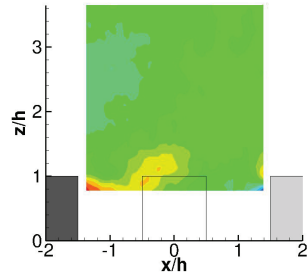
c)



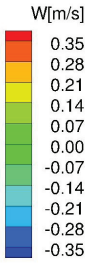
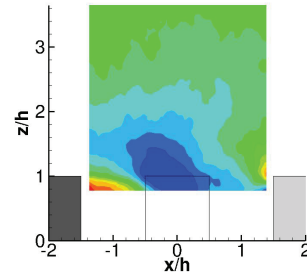
d)



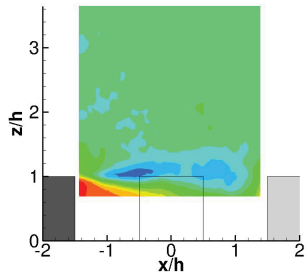
e)



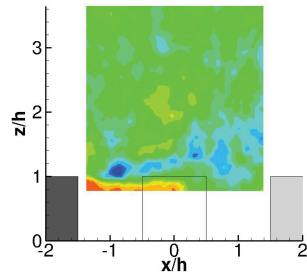
f)



g)



h)



i)

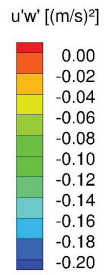
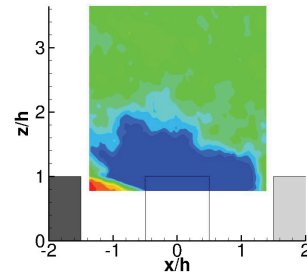


Figure 3.4: Comparison of maps of the one-point statistics: the two in-plane components of the mean velocity, $\langle u \rangle$ and $\langle w \rangle$ (first and second rows), and the Reynolds shear stress $\langle u'w' \rangle$ (last row), from full ensemble averages (first column) and conditioned by the two configurations (positive tilt and negative tilt, respectively second and third columns).

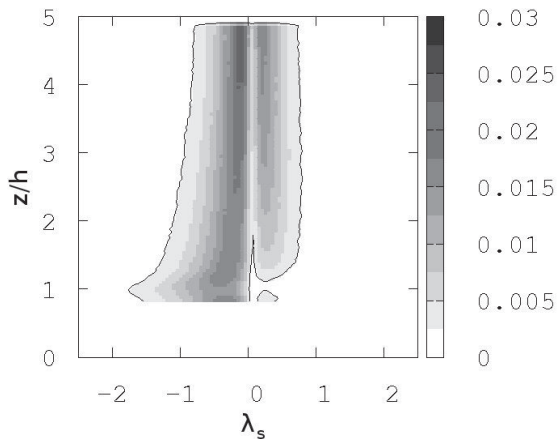


Figure 3.5: PDF of λ_s as a function of normalized height z/h .

exist in the whole part of the observed flow, with more negative λ_s vortices than positive, in agreement with the mean shear imposed by the BL flow. While numbers of positive and negative λ_s vortices seem constant above the RSL, the negative λ_s vortices tend to be more numerous in the RSL and below, and become the vast majority of the vortical structures near the canopy top ($z/h = 1$). Combining observations of fluctuating velocity fields and maps of λ_s , it appears that strong clockwise rotating vortices are strongly related to the shear layer originating from the top of the roughness elements. These vortices are characterized by a large value of swirling strength such that λ_s can reach -2 at canopy top level. Thus, in order to extract only these strong negative vortices, a threshold is fixed at -1.3 . Figures 3.6 and 3.7 show two examples of this extraction scheme for two different fluctuating velocity fields. It appears that these strong clockwise rotating vortices (gray patches in Fig. 3.6 and 3.7) shed from the canopy top and intermittently released toward the RSL by the upward flapping can "survive" long enough to be convected downstream, in and above the RSL. The RSL is defined as being the sublayer in which the BL flow is dynamically influenced by the presence and length scales of roughness elements. So, one can expect to find such vortices in this sublayer while finding them above in the inertial sublayer is more surprising.

4 CONCLUSION

In the present study, a full-depth simulation of a suburban boundary layer above an idealized

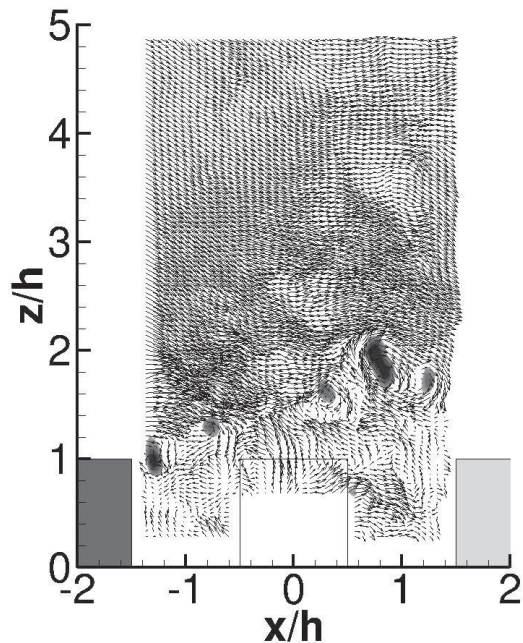


Figure 3.6: Example of application of the extraction scheme (gray patches: thresholded negative λ_s) for an positive tilt shear layer axis.

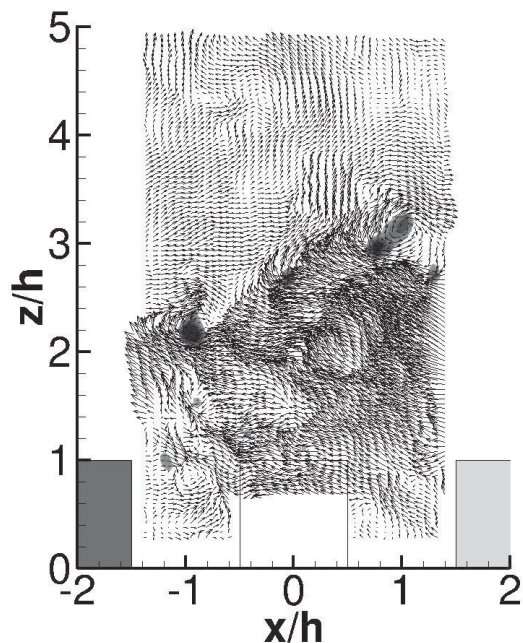


Figure 3.7: Detection of high negative λ_s vortices above the RSL. These vortices have been shed from upstream obstacles out of field of view.

canopy model was performed in a wind tunnel. In order to elucidate the spatio-temporal interactions between the atmospheric boundary layer and the urban canopy flows, measurements in a stream-wise aligned vertical plane of the three components of the instantaneous velocity were performed via Stereoscopic PIV.

Existence of a two-scale behaviour of the flow was confirmed, one of which being characteristic of the boundary layer flow and the other one of the canopy layer flow. At the interface between these two flows, the high shear layer created downstream of the top of a roughness element was analysed. It was found that the flapping behaviour of this shear layer is related to the height and arrangement of the roughness elements, and influences the roughness sublayer height. The one-point statistics, in the canopy layer and the roughness sublayer, depend on the flapping tilt angle. A shear layer with a negative tilt is correlated with a large penetration of the boundary layer flow from upstream into the canopy layer confirming the top-down influence between the two flows. In the opposite case, with a positive tilt, the shear layer is correlated with the emergence of the canopy layer flow towards the roughness sublayer. In the two cases, the shear layer is correlated with the presence of strong clockwise rotating vortices released by the canopy top and inducing Q2 and Q4 events. Existence of numerous Q2 events in the roughness sublayer is associated to the dissemination of these vortices via the flapping shear layer. The majority of Q4 events is associated to the boundary layer flow dynamics, which explains their large contribution to the Reynolds shear stress. Nevertheless, results have shown that the vortices from the canopy top can populate sublayers above the roughness sublayer creating numerous local perturbations for the boundary layer flow.

Future work will extend this analysis to the horizontal planes at the level of both the roughness and inertial sublayers, in order to investigate the behaviour of the statistics and the dissemination of the vortices along the transversal direction.

References

- Adrian, R. J., K. T. Christensen, and Z.-C. Liu, 2000a: Analysis and interpretation of instantaneous turbulent velocity fields. *Exp. Fluids*, **29**, 275–290.
- Adrian, R. J., C. D. Meinhart, and C. D. Tomkins, 2000b: Vortex organization in the outer region of the turbulent boundary layer. *J. Fluid Mech.*, **422**, 1–54.
- Adrian, R. J. and J. Westerweel, 2010: *Particle Image Velocimetry*. Cambridge University Press.
- Castillo, M. C., A. Inagaki, and M. Kanda, 2011: The effects of inner- and outer-layer turbulence in a convective boundary layer on the near-neutral inertial sublayer over an urban-like surface. *Boundary-Layer Meteorol.*, **140**, 453–469.
- Castro, I. P., H. Cheng, and R. Reynolds, 2006: Turbulence over urban-type roughness : deductions from wind-tunnel measurements. *Boundary-Layer Meteorol.*, **118**, 109–131.
- Coceal, O., A. Dobre, and T. G. Thomas, 2007a: Unsteady dynamics and organized structures from DNS over an idealized building canopy. *Int. J. Climatol.*, **27**, 1943–1953.
- Coceal, O., A. Dobre, T. G. Thomas, and S. E. Belcher, 2007b: Structure of turbulent flow over regular arrays of cubical roughness. *J. Fluid Mech.*, **589**, 375–409.
- Counihan, J., 1969: An improved method of simulating an atmospheric boundary layer in a wind tunnel. *Atmos. Environ.*, **3**, 197–214.
- ESDU, 1972: Characteristics of wind speed in the lower layers of the atmosphere near the ground: strong winds (neutral atmosphere). *Engineering Sciences Data Unit 72026*.
- Hunt, J. C. and J. F. Morrison, 2000: Eddy structure in turbulent boundary layers. *Euro J. Mech. B – Fluids*, **19**, 673–694.
- Hutchins, N., W. T. Hambleton, and I. Marusic, 2005: Inclined cross-stream stereo particle image velocimetry measurements in turbulent boundary layers. *J. Fluid Mech.*, **541**, 21–54.
- Hutchins, N. and I. Marusic, 2007: Evidence of very long meandering features in the logarithmic region of turbulent boundary layers. *J. Fluid Mech.*, **579**, 1–28.
- Inagaki, A., 2008: Atmospheric turbulence over an array of massive cubes. Ph.D. thesis, Department of International Development Engineering, Tokyo Institute of Technology, Tokyo, Japan.

- Inagaki, A., M. C. L. Castillo, Y. Yamashita, M. Kanda, and H. Takimoto, 2012: Large-eddy simulation of coherent flow structures within a cubical canopy. *Boundary-Layer Meteorol.*, **142**, 207–222.
- Inagaki, A. and M. Kanda, 2010: Organized structure of active turbulence over an array of cubes within the logarithmic layer of atmospheric flow. *Boundary-Layer Meteorol.*, **135**, 209–228.
- Irwin, H., 1981: The design of spires for wind simulation. *J. Wind Eng. Ind. Aerodyn.*, **7**, 361–366.
- Kanda, M., 2006: Large-eddy simulations on the effects of surface geometry of building arrays on turbulent organized structures. *Boundary-Layer Meteorol.*, **118**, 151–168.
- Kanda, M., R. Moriwaki, and F. Kasamatsu, 2004: Large eddy simulation of turbulent organized structure within and above explicitly resolved cubic arrays. *Boundary-Layer Meteorol.*, **112**, 343–368.
- Krogstad, P.-A. and R. Antonia, 1999: Surface roughness effects in turbulent boundary layers. *Exp. Fluids*, **27**, 450–460.
- Marusic, I., B. J. McKeon, P. A. Monkewitz, H. M. Nagib, A. J. Smits, and K. R. Sreenivasan, 2010: Wall-bounded turbulent flows at high reynolds numbers: Recent advances and key issues. *Phys. Fluids*, **22**, 065 103.
- Perret, L. and T. Ruiz, 2012: *Coherent Structures in Flows at the Earth's Surface*, chap. SPIV analysis of coherent structures in a vegetation canopy model flow. John Wiley and Sons, in press.
- Raupach, M. R., 1981: Conditional statistics of reynolds stress in rough-wall and smooth-wall turbulent boundary layers. *J. Fluid Mech.*, **108**, 363–382.
- Reynolds, R. T. and I. P. Castro, 2008: Measurements in an urban-type boundary layer. *Exp Fluids*, **45**, 141–156.
- Standen, N., N. A. E. (Canada), N. A. E. C. L. S. A. Section, and N. R. C. of Canada, 1972: *A Spire Array for Generating Thick Turbulent Shear Layers for Natural Wind Simulation in Wind Tunnels*. -. Laboratory technical report, National Aeronautical Establishment, Low Speed Aerodynamics Section.
- Takimoto, H., A. Sato, J. F. Barlow, R. Moriwaki, A. Inagaki, S. Onomura, and M. Kanda, 2011: PIV measurements of turbulent flow within an outdoor urban scale model and flushing motions in urban canopy layers. *Boundary-Layer Meteorol.*, **140**, 295–314.
- Tomkins, C. D. and R. J. Adrian, 2003: Spanwise structure and scale growth in turbulent boundary layers. *J. Fluid Mech.*, **490**, 37–74.
- Townsend, A. A., 1956: *The Structure of Turbulent Shear Flow*. Cambridge University Press.